Earth Planet. Sci. Lett. 685 (2026) 120030

Contents lists available at ScienceDirect

Earth and Planetary Science Letters

journal homepage: www.elsevier.com/locate/epsl

Earthquake-induced dolomite decarbonation in the Dinar Fault Zone, western Türkiye

Cecilia Viti [a,*], Telemaco Tesei [b], Andrea Brogi [c,d,e], Richard Spiess [b], Domenico Liotta [c], M. Cihat Alçiçek [f]

[a] Department of Physics, Earth and Environmental Sciences, University of Siena, Siena, Italy
[b] Department of Geosciences, University of Padova, Padua, Italy
[c] Department of Earth and Geo-environmental Sciences, University of Bari Aldo Moro, Bari, Italy
[d] CRUST, Centro inteRUniversitario per l'analisi Sismotettonica Tridimensionale (interUniversity Centre for Three-Dimensional Seismotectonic Analysis), Chieti, Italy
[e] OGS, National Institute of Oceanography and Applied Geophysics, Trieste, Italy
[f] Department of Geology, University of Pamukkale, Denizli, Türkiye

ARTICLE INFO

Editor: J.P. Avouac

Keywords:
Dinar fault zone
Seismic slip
Frictional heating
Dolomite decarbonation
Calcite nanograins

ABSTRACT

This work reports a multiscale study of the Dinar fault zone, focusing on a normal fault, hosted in Triassic dolostone, that is part of the fault system responsible for the 1995 Dinar earthquake (Mw = 6.2). Mirror surfaces are associated with the seismogenic fault zone, suggesting a relationship with the processes occurring during earthquakes. The investigation of mirror surfaces, from the outcrop to the micro- and nanoscale (i.e., high-resolution TEM imaging and electron diffraction) provided unambiguous evidence of dolomite thermal decomposition, occurring at ~ 550 °C, with formation of Mg-rich calcite nanograins and amorphous alumosilicatic material, possibly deriving from minor phyllosilicates in host dolostones. Our observations are in perfect agreement with high-velocity experiments on dolomite, which produces identical mineralogical assemblages and nanostructures. The Dinar case study represents a unique example, as it provides the first unequivocal evidence of dolomite decomposition associated to a mirror along the fault plane of a known seismogenic structure, likely formed during the coseismic slip compatible with the magnitude historical earthquakes in the region, including the 1995 Dinar earthquake.

1. Introduction

Fault rocks preserve invaluable information about earthquake mechanics and may allow the identification of seismogenic faults in the field. Specific rock assemblages provide information about the rupture propagation (e.g., Griffith et al., 2010) and slip style (e.g., seismic or aseismic and the shades of grey in between, Rowe and Griffith, 2015 for a comprehensive review). In this general framework, carbonate-hosted faults are key targets for investigating earthquake-related fault rocks, as they accommodate the nucleation and propagation of many continental and destructive earthquakes all over the world (Burchfiel et al., 2008; Valoroso et al., 2014; Bernard et al., 2006). However, although carbonate rocks are abundant in seismogenic settings, the classic unambiguous markers of co-seismic rupture propagation and fast slip, i.e., pseudotachylite, have only once been tentatively described for this type of rocks (e.g., Viganò et al., 2011). In carbonatic rocks, the most reliable indicators for seismic rupture and slip are considered to be shattered and pulverized rocks (e.g., Fondriest et al., 2013) fluidized cataclasites (Rowe et al., 2012; Tesei et al., 2013), fault mirrors (Smith et al., 2013; Siman-Tov et al., 2013; Fondriest et al., 2013), and products of thermal decomposition (e.g., Rowe et al., 2012; Collettini et al., 2013, 2014).

Among these indicators, mirror fault surfaces (MFS) are shiny and localized slip zones reflecting the light due to their extremely smooth surface, commonly coated by ultrafine-grained layers of nanoparticles or amorphous material (Power and Tullis, 1989; Siman-Tov et al., 2013; Kirkpatrick et al., 2013). MFS have been inferred to mark extremely localized and fast (seismic) fault slip, mostly by resemblance to shiny surfaces produced during high slip velocity experiments (e.g., Han et al., 2010; Smith et al., 2013; Fondriest et al., 2013; De Paola et al., 2011; Pozzi et al., 2019). However, in some cases MFS are also produced in experiments where the slip velocity was much lower (μm/s) than the seismic slip rates, calling into question the reliability of this indicator (e.

* Corresponding author at: University of Siena, Italy.
E-mail address: cecilia.viti@unisi.it (C. Viti).

https://doi.org/10.1016/j.epsl.2026.120030
Received 24 November 2025; Received in revised form 24 March 2026; Accepted 30 March 2026
Available online 10 April 2026

g., Verberne et al., 2014; Tesei et al., 2017).

Potentially, the association of MFS with other microstructures, such as fluidized cataclasites and thermal decomposition products (Tesei et al., 2013; Coppola et al., 2021), or localized plastic deformation (Smith et al., 2013; Pozzi et al., 2019), may yield sufficient evidence of past seismic slip. In fact, thermal decomposition of carbonates induced by fast fault slip and frictional heating is considered an unambiguous co-seismic process (Collettini et al., 2013; Rowe et al., 2015). It has the

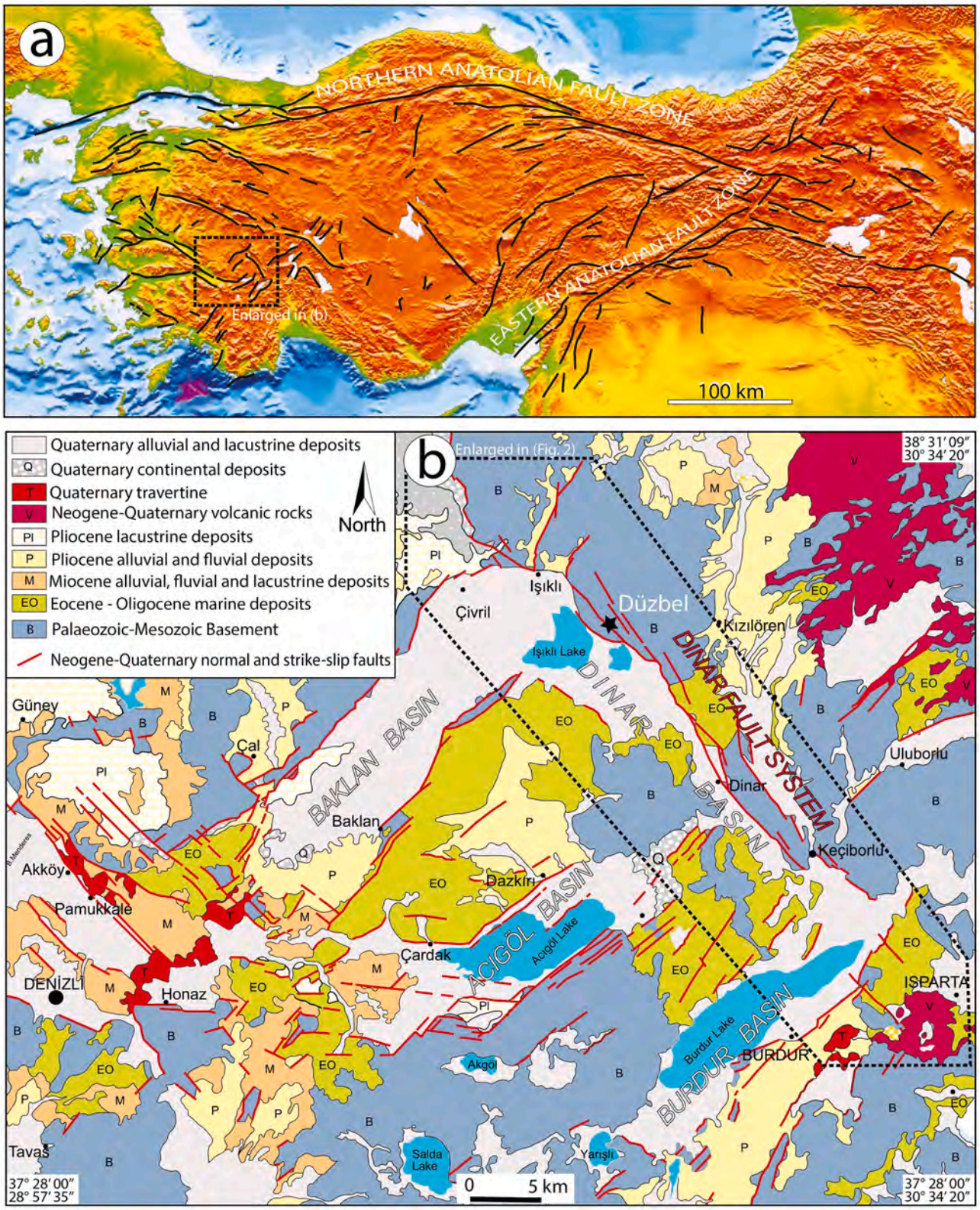

Fig. 1. (a): Satellite image of the Anatolia peninsula with highlighted the main regional structures. The sector encompassing Dinar Fault system is squared and enlarged in (b): Schematic geological map illustrating the structural relations between the Dinar Fault System and the Quaternary continental basins (after Alçiçek et al. 2013, modified).

effect of buffering the temperature rise on the fault surface, hence preventing frictional melting, and release of CO_2 -rich fluids that reduces the effective stress on the fault. Thermal decomposition and its effect on fault slip are also well constrained by theoretical models (Rice, 2006; Sulem and Famin 2009) and reproduced by high velocity experiments in both calcite and dolomite (Han et al., 2010; De Paola et al., 2011).

A few examples of thermal decomposition associated to fast slip have been reported in natural contexts, either along the surface of large faults (Collettini et al., 2013, 2014; Rowe et al., 2012; Coppola et al., 2021) or in catastrophic large landslides (e.g., Beutner and Gerbi, 2005; Mitchell et al., 2015). However, none of the documented examples is unambiguously associated to faults with known recent seismic activity.

In this work we present the results of a study carried out on the Dinar Fault zone (Anatolia, Türkiye), i.e., a carbonate seismogenic fault zone, tens of kilometers in length, with multiple fault surfaces, which has caused earthquakes in the past and in the present. Along the Dinar fault Zone (DFZ), we investigated the fault rocks and associated mirror surfaces associated to the normal fault system responsible for the 1995 Dinar earthquake ($M_w = 6.2$; Özalp et al. 2018), developed in dolostone host rocks. Our results show that the mirror surface and the principal slip surfaces were unambiguously related to thermal decomposition processes, triggered by an active fault system that produces moderate magnitude earthquakes. The DFZ case history is particularly significant because it documents deformation features in a natural seismogenic

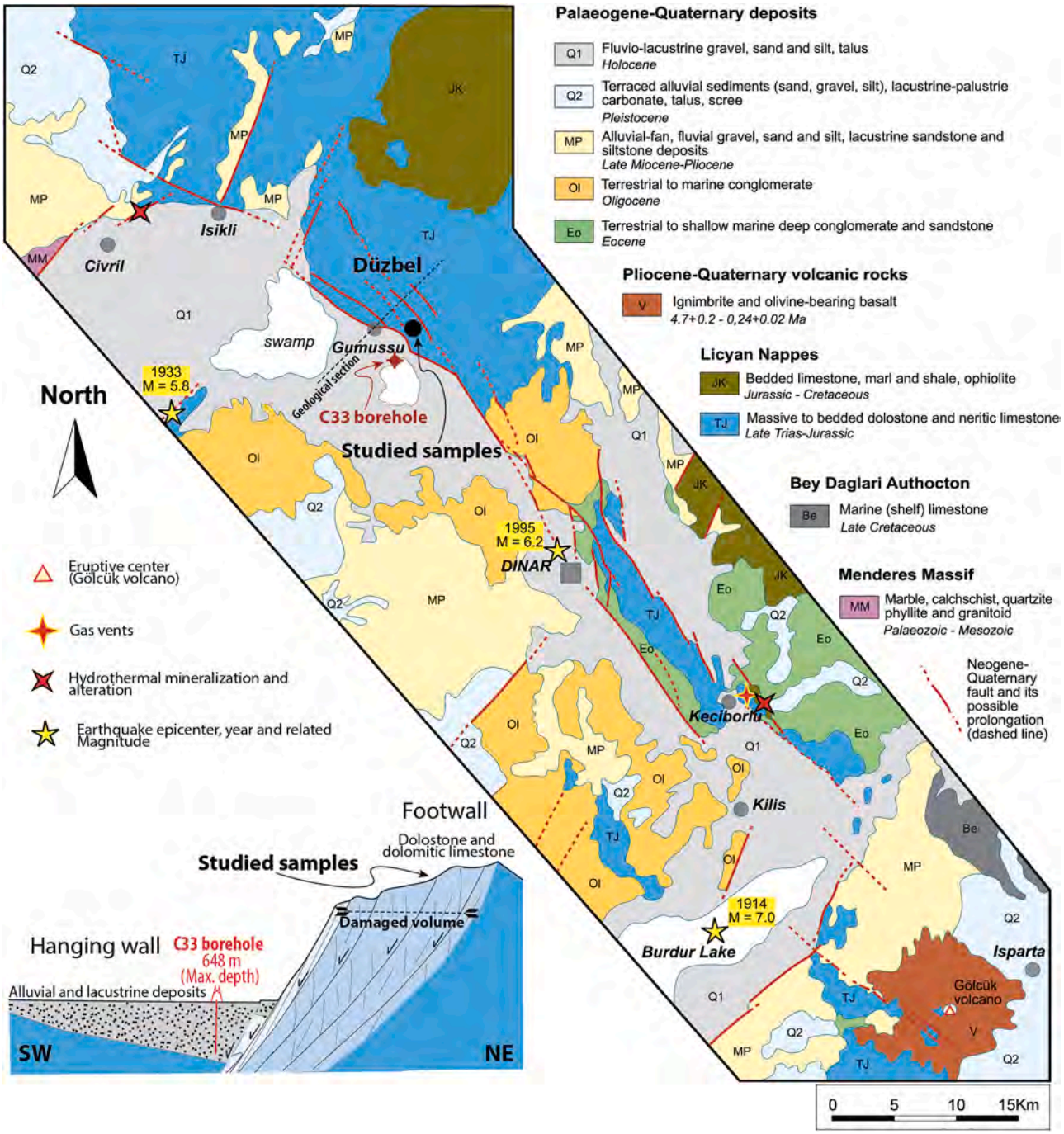

Fig. 2. Geological map of the Dinar Fault System showing the structural location of the study samples (after Alçiçek et al. 2013, modified) and the epicentral location of the most recent earthquakes (after Özalp et al., 2018). The location of borehole Ç33 is also indicated: this drilled 648 m of Quaternary sediments without reaching the substratum (after Sezgin, 2020).

fault zone affecting dolostone, associated with a seismic event of known magnitude, previously observed only in laboratory experiments.

2. Geological and seismotectonic setting

The Dinar Fault Zone (DFZ) is a ~100 km long fault located in the southwestern part of the Anatolian Peninsula, Türkiye. It is marked by a NW-SE striking, SW dipping regional fault defining the northeastern margin of the Quaternary Dinar Basin (Fig. 1) and crosscuts the SW-NE trending Late Miocene-Pliocene Basins (Alçiçek et al. 2013) which developed during the post-collisional extensional tectonics following the Alpine orogeny (Şengör and Yılmaz, 1981).

The switch from compressional to extensional tectonics occurred during the latest Oligocene- Early Miocene (~25 Ma) time interval, because of changes in the Africa-Eurasia plate convergence (Ten Veen et al. 2009). Although extension in southwestern Anatolia is still active, it is generally subdivided into two main phases: a former Miocene phase dominated by low-angle detachment faults, and a later Pliocene-Quaternary phase characterized by high-angle normal faults. These latter formed syn-tectonic continental basins bounded by active normal faults with high seismogenic potential (Mw > 7; Alçiçek et al., 2013).

The DFZ has experienced changes in kinematics over time. During the Late Miocene-Pliocene, it played the role of a transfer fault zone accommodating differential extension between the Baklan, Acıgöl, and Burdur basins (Alçiçek et al., 2013). During the Quaternary it was reactivated as a normal fault zone, laeding to the development of the Dinar Basin and promoting the activity of the coeval Gölcük volcanic complex along the southern margin of the fault zone (Platevoet et al., 2008). Regional uplift in the surrounding areas is estimated to be about 400 m since middle Pliocene, not considering fault activity (Westaway et al., 2004). Therefore, considering: (i) this estimated uplift also for the Dinar area; (ii) at least 648 m of Quaternary sediments, resting on the hangingwall were drilled by the Turkish Geological Survey in 2010 (Figs. 2 and 1s) without reaching the substratum (Sezgin, 2020); (iii) the topmost altitude of the footwall is at about 1600 m a.s.l while hangingwall is at about 850 m a.s.l., a Quaternary exhumation of the Dinar fault system exceeding 1.4 km is the minimum reasonable value. Similarly, Özalp et al. (2018) estimated a Quaternary vertical throw between 1600 and 1100 m, by assuming only 200 m of Quaternary sediments.

The DFZ is one of the active seismogenic structures in the region, as demonstrated by the destructive earthquake of October 1st, 1995 (Mw = 6.2: Fig. 2), known as the Dinar earthquake (Özalp et al., 2018, and references therein). This event caused 90 fatalities, hundreds of injures, and severe damage to over 4000 buildings (Tezkan and İpek, 1996; Öncel et al., 1998; Utkucu et al., 2002).

The epicenter was located along a DFZ segment that juxtaposes the Quaternary basin-fill sediments of the Dinar Basin (an ~70 km long and ~10 km wide structural depression) to the Triassic dolostone and dolomitic limestone of the Licyan Nappe (Alçiçek et al., 2013). Co-seismic surface ruptures and ground cracks were mostly observed in the hanging wall of the DFZ (Koral, 2000; Özalp et al., 2018), with ground-level offsets of up to 60 cm (Fig. 2).

The fault scarps are well exposed in the footwall, where the Triassic dolostone and dolomitic limestone are exposed, along with limited exposures of Paleozoic micaschist, quartzite, and marble, belonging to the Menderes Massif. The faults damage zone is several hundred meters thick, consistent with the long-lived tectonic activity of the structure. Late Quaternary deformation is localized along the main fault scarp, where surface ruptures from the 1995 earthquake are still preserved. The fault scarp is characterized by subparallel fault surfaces and cataclastic bands enclosing up to 3 m thick lithons of intensely damaged rock, exposed as discontinuous patches. Kinematic indicators such as tool marks, chatter marks, and slickensides are common kinematic indicators, displaying pitches ranging from 70° to 110° (Fig. 1s).

3. Experimental methods

X-ray diffraction (XRD) on powder bulk host-rock was performed by a Philips X'Pert PRO PW 3040/60 with X'Celerator PW 3015 detector, allowing bulk mineralogical composition of the host rock. Thin petrographic sections, parallel and perpendicular to the main fault surface embedded in the study samples from the Dinar Fault Zone, were observed by polarized light Optical Microscopy (OM), Scanning Electron Microscopy (SEM) and Transmission Electron Microscopy (TEM). SEM was equipped with an energy dispersive spectrometer (EDS - Thermofisher Pathfinder X-ray Microanalysis System), providing chemical analysis for atoms heavier than C. Backscattered (BSE) and secondary electrons (SE) were used for imaging, both for polished petrographic thin sections and untreated fault surface (only carbon-coated without polishing).

TEM investigations were performed by a JEOL 2010 microscope, working at 200 kV, with ultra-high resolution (UHR) pole piece and point-to-point resolution of 0.19 nm. The microscope is equipped with an ultra-thin window energy dispersive spectrometer (EDS ISIS Oxford). Data were recorded by an Olympus Tengra CCD camera. TEM grids were picked from petrographic cross sections and were thinned by Ar^+ ion milling using both Gatan Dual Ion Mill and Precision Ion Polishing System (PIPS). This multiscale microscopic investigation (from MO to high-resolution TEM) allowed careful characterization of the micro-nanostructures and mineral reactions occurring at the mirror fault surface. The availability of microanalytical chemical compositions (by SEM/EDS and TEM/EDS), coupled with TEM diffraction data, allowed the accurate identification of all mineral phases, even when submicrometer in size. TEM non-specialist readers may refer to Viti (2011) for basic knowledge about TEM image formation and selected area electron diffraction (SAED).

EBSD analyses were performed to get information about grain size distribution and possible crystal preferred orientation on the mirror fault surface. EBSD maps were acquired with a Tescan-Solaris FEG-FIB SEM equipped with a Symmetry2 EBSD detector (Oxford Instruments). For acquisition an accelerating voltage of 20 KV, a beam current of 10 nA and step sizes of 0.5 to 2 μm have been used, whereas post-processing has been done with the AZtecCrystal 3.1 software (Oxford Instruments). No carbon coating was used, but conductivity of the analyzed area was established by application of a carbon band bandage around the analyzed rectangular area. Because misindexing was common using a dolomite match unit due to pseudosymmetry problems, we have mapped both Mg-rich and Ca-rich carbonates as magnesian calcite, consistent with the suggestion of Pearce et al. (2013).

4. Characteristics of host rock and mirror fault surface

The mirror fault surface (MFS) analyzed in this study comes from the Triassic dolostone near the village of Düzbel, ~20 km north of Dinar, within the fault damage zone and just a few tens of meters from the main fault scarp (Figs. 1 and 2), where minor faults, fractures and calcite veins are also present. The regional main fault plane consists of a polished surface with local black mirror-like spots with clear striations (Fig. 3). Fault is steeply dipping toward SW (70°) and strikes 120°

Thin sections for petrographic analyses have been prepared perpendicular to the MFS to detect possible microstructural and mineralogical changes from the host rock towards the fault surface (e.g., scanned thin section shown in Fig. 4a). The host rock is a cataclasite, consisting of randomly oriented dolomite crystals, with grain size between 20 and 50 μm. Based on bulk XRPD data, dolomite is the only rock-forming mineral and no other crystalline phase has been detected, at least within the experimental detection limits. Stylolite surfaces are rare, whereas coarse dolomite veins pervasively occur in all samples (e.g., the transparent, uncolored features in Fig. 4a and high-birefringence vein in Fig. 4b). Secondary slip zones, with localized grain size reduction, may develop within the host rock, parallel to the main fault surface

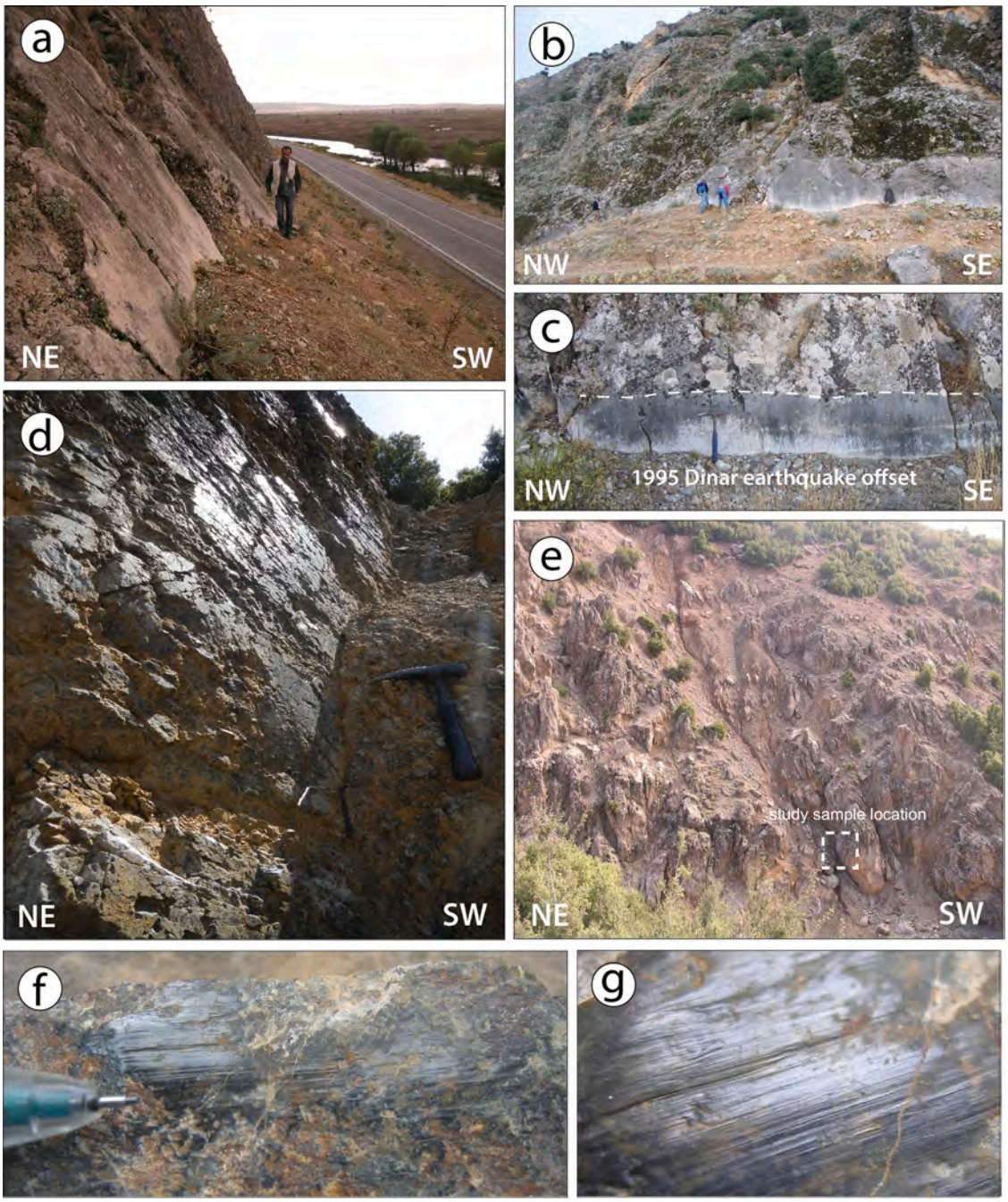

Fig. 3. a) Panoramic view of a fault segment belonging to the Dinar fault system; b-c) Detail of the fault offset that developed during the October 1995 earthquake; d) Detail of the shiny fault surface, showing a clear mirror effect; e) Fault zone near the village of Düzbel, from which the analyzed samples were collected (dashed square); f-g) Details of the analyzed samples taken from the fault zone shown in photo (e). These samples were photographed on a desk; therefore, the orientation of the kinematic indicators does not correspond to their in-situ setting.

(e.g., black arrows in Fig. 4c and d), or with synthetic shear fractures, indicating reactivation of the already cemented fault plane.

The principal slip surface is locally very sharp and planar (dashed black line in Fig. 4a) and in these portions it corresponds to the MFS observed at the meso-macroscale (Fig. 3). At the optical microscope resolution, no mineralogical-microstructural modifications appear to occur in the host rock approaching the MFS, where only truncated dolomite grains may be observed. The MFS is typically associated with a coarse-grained dolomite vein, locally showing a preferential occurrence of ultrafine brownish material (upper side in Fig. 4e).

Fig. 5 reports representative SEM/BSE images of the MFS, in parallel (a and b) and cross-section (c-f) orientations. In particular, Fig. 5a and b compare the dolostone host-rock (artificially polished surface parallel to the MFS and ~ 1 cm below the MFS) and the natural MFS (untreated and unpolished surface), respectively. Dolomite grain size appears to be almost unchanged between host rock and MFS, but overall microstructure is significantly different. Dolomite single grains in the MFS exhibit inner contrast heterogeneities, possibly suggesting subgrain boundaries and incipient grain size reduction. One of the most important microstructural differences regards dolomite habit and grain boundaries, euhedral and sharp in the host rock (Fig. 5a) vs. lobate and interpenetrating in the MFS (Fig. 5b). Dolomite grains in the MFS are also characterized by the pervasive occurrence of intracrystalline porosity (e.g., inset in Fig. 5b).

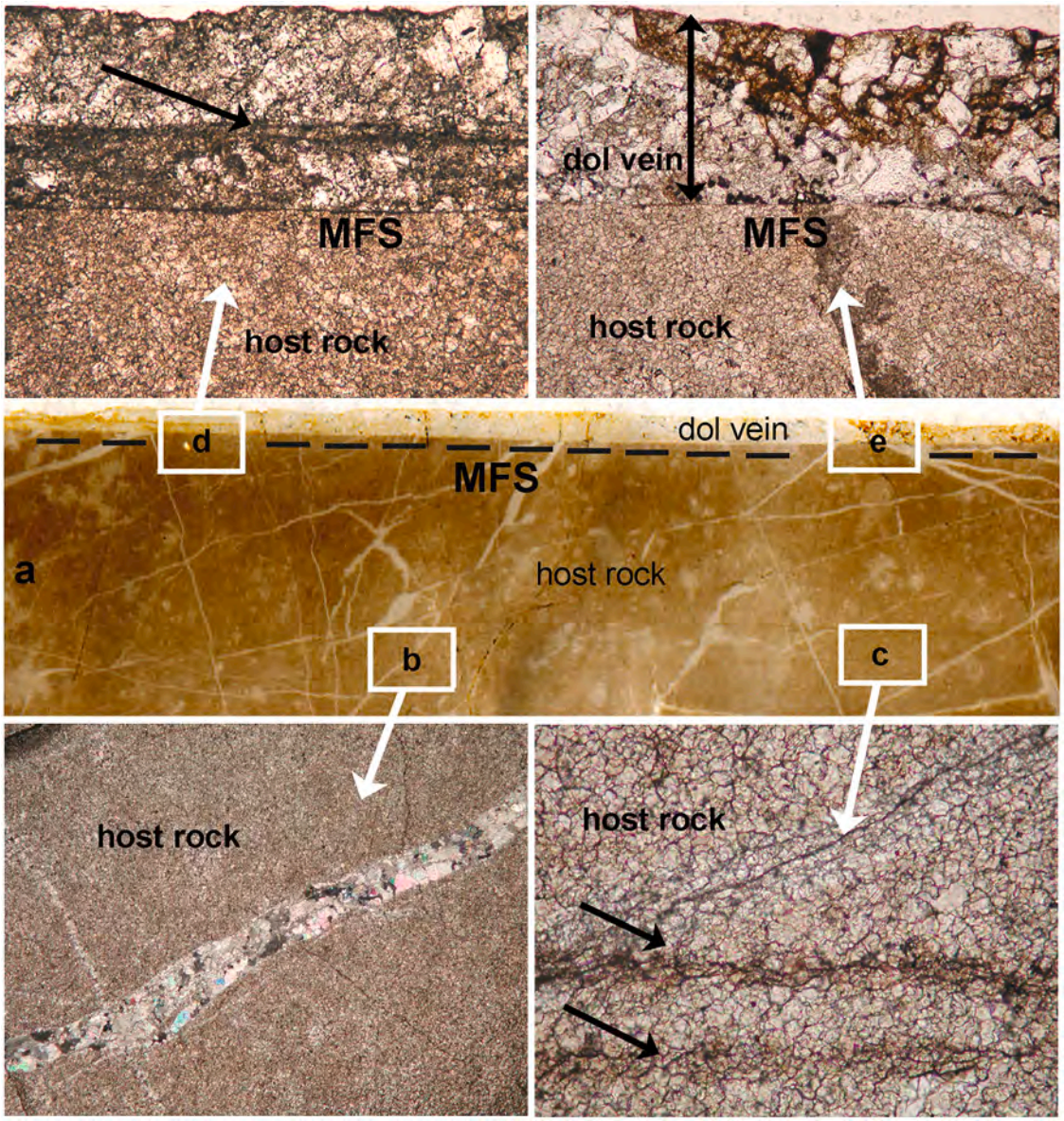

Fig. 4. Representative fault-rock sample (a, scanned petrographic section) showing the relationships between dolostone host rock, principal slip surface (MFS) and a late dolomite coarse vein. Localized grain size reduction and development of Riedel shears indicating right-lateral sense of slip are also evident. The host rock is crosscut by several coarse-grained dolomite veins (detail in b, plane polarized light, crossed nicols image) and by "secondary" subparallel slipping zones, parallel to the MFS (e.g., black arrows in c). Figures d and e show details of the MFS, highlighting the common occurrence of subparallel secondary slipping surfaces and of coarse-grained dolomite vein (dol vein), respectively (plane polarized light, one nicol images).

To better understand the mechanisms operating during the formation of the MFS, EBSD data have been acquired from a rectangular (2043 μm x 767 μm) portion of the MFS showing striations oriented parallel to the long axis of the rectangle (X direction in the maps). We remind that EBSD patterns are believed to generate usually near the analyzed sample surface, typically in a depth range of 10 nm (Dingley 2004). EBSD maps and BSE images need not strictly matching one to one, even when acquired both in the MFS, since BSE signal reaches the detector form a deeper depth into the sample than the diffracted backscattered electrons (Rau and Reimer, 2001). The EBSD-map shown in Fig. 6a, with a base length of 500 μm, is a quarter of the whole EBSD map acquired with a step size of 2 μm. In Fig. 6aa white rectangle outlines Fig. 6b which is a higher resolution map and has been acquired with a step size of 500 nm. Inverse Pole Figure (IPF) color coding parallel to X has been used for both maps, and in both of them "small grains" are highlighted by brighter colors. "Small grains" arrange along grain boundaries of "large grains", at triple and four grain contacts of "large grains", and occasionally inside "large grains". The "large grains" have usually no free interspaces along their contacts, show generally straight to lobate, rather subordinately sutured grain boundaries, and not uncommonly grain boundaries support impingement between grains; "small grains" have typically serrated grain boundaries. "Small grains" form also patches of clustered grains and typically cavities between grains occur. Fig. 6c shows area distribution diagrams of small and large grains. "Small grains" (Fig. 6c) form a maximum which suddenly decreases from 0,75 to 5 μm^2, then progressively grain counts approximate zero at 24.83 μm^2. "Large grains" (Fig. 6d) reach the maximum at 25 μm^2, from here grain counts decrease suddenly to about 60 μm^2 and then progressively approach zero grain counts at 126 μm^2. This binary distribution in grain size is evident within the EBSD maps.

Focusing on the crystallographic mismatch between neighbor grains, the EBSD maps reveal that 80 % of the grain-grain contacts are characterized by $> 20^\circ$ misorientations (black colored grain boundaries). The misorientation distribution diagrams (Fig. 6e and f) show a peak

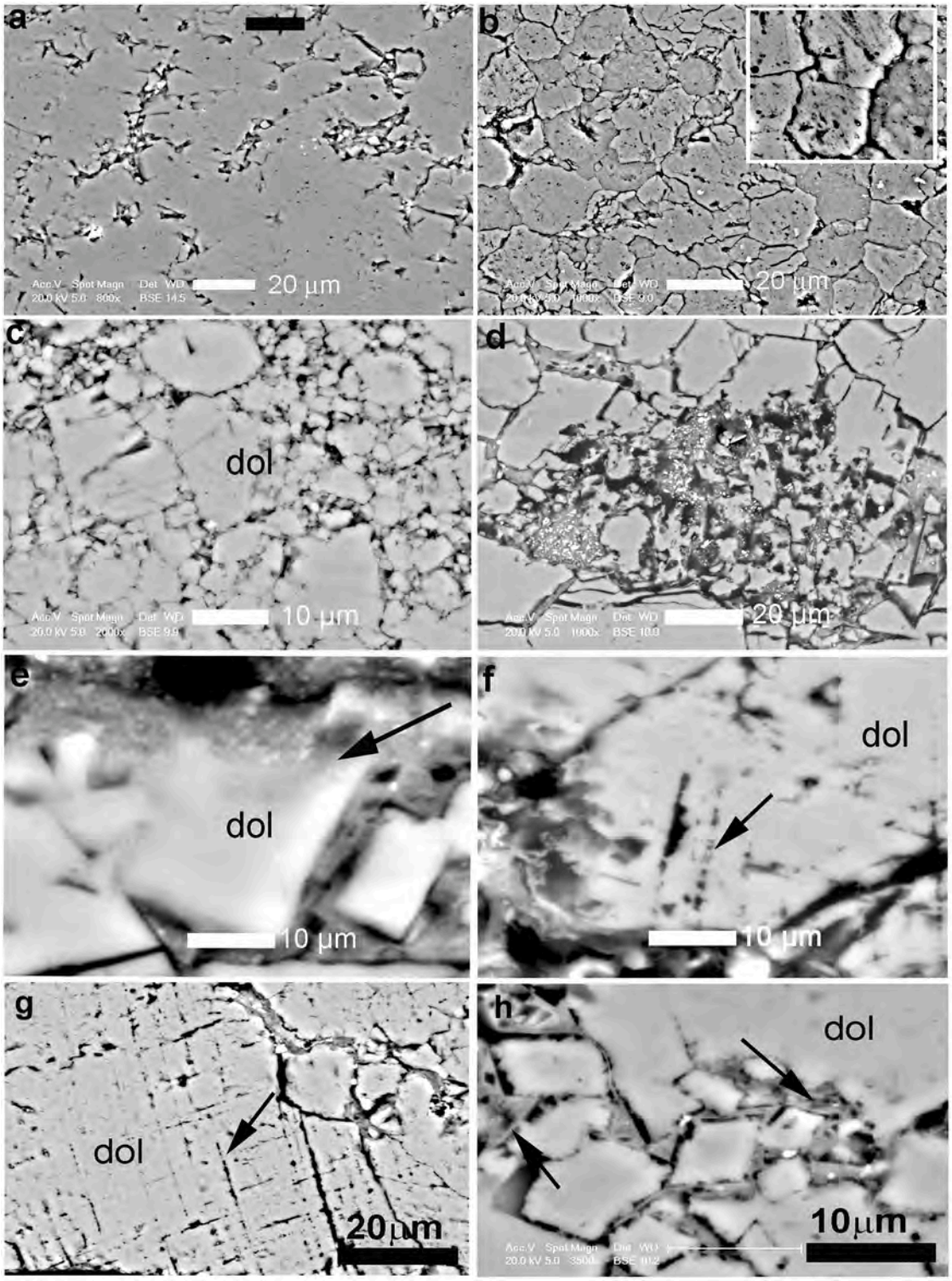

Fig. 5. SEM/BSE images of (a) artificially polished surface of the host dolostone (1 cm below and parallel to the MFS), and (b) natural MFS (without polishing), with interpenetrated grain boundaries and abundant intracrystalline porosity (inset). From (c) to (h) SEM/BSE images from cross section polished samples, showing main dolomite microstructures at the MFS. In particular, (c) grain size reduction to the micron scale; (d) strongly anhedral dolomite grains, with lobated and embayed boundaries; (e) partial reaction of a dolomite crystal, replaced by ultrafine material (arrow); (f) and (g) preferential occurrence of pores along cleavage and twinning planes; (h) occurrence of skeletal crystals (arrow) in the intergranular space.

both for the "small grains" as well as for the "larger grains" between 5 and 20° misorientation, whereas the bulk of the grain boundaries follow closely the trend of a random misorientation angle distribution. No preferred crystallographic orientation is suggested by the Inverse Pole Figures (IPF) constructed for the "small grains" and the "large grains" parallel to X (Fig. 6g and h). The "small grains" form several maxima distributed within a broad girdle showing a slightly less density of widely dispersed crystallographic directions. The "larger grains" form one maximum close to the crystallographic direction <20-21> which is immersed in a broad field of not well-defined crystallographic

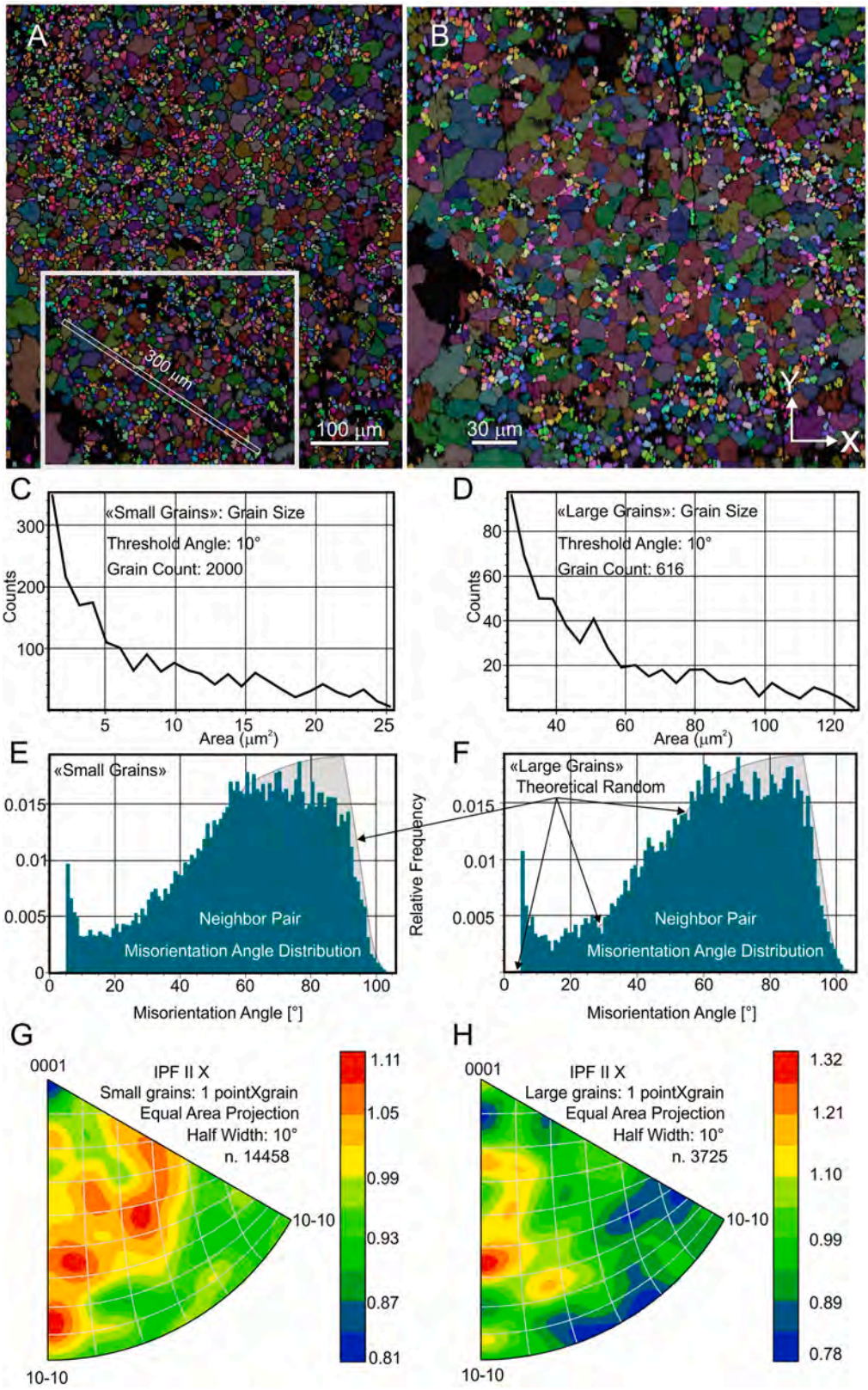

Fig. 6. EBSD analysis: (a) EBSD map acquired with a step size of 2 µm (a quarter of the whole map is shown). Highlighted grains are "Small Grains (see 7c for grain size distribution). White rectangle refers to Fig. b, a high resolution EBSD Map. Color-coding according IPF parallel to X. (b) A binary distribution between "small grains" and "large grains" is evident (compare 7c with 7d for grain size distribution). In addition, a ghost of a very large rectangular clast (about 300 µm long), completely recrystallized to "large grains", is recognized. Several such clasts occur in the whole acquired EBSD map. (c) and (d) Grain size distribution of "small-" and "large grains". (e) and (f) Misorientation angle distribution of "small" and "large" grains. Eighty percent of the neighbor grains follow the theoretical random distribution. (g) and (h) Inverse Pole Figures (parallel X) for "small-" and "large grains" confirm no crystallographic preferred orientation for both grain types.

directions.

5. Deformation microstructures and decarbonation process

Deformation microstructures and possible decarbonation evidence have been investigated by SEM and TEM, from the micron- to the nanometer scale, mostly focusing on the MFS and immediately surrounding dolostone. Approaching the MFS, dolomite crystals exhibit peculiar microstructures that are absent in the host rock and can be therefore interpreted as related to deformation and slip movement. Fig. 5c–h report a summary of most recurrent microstructures, observed in cross-petrographic sections of the fault zone. Dolomite crystals exhibit grain size reduction down to the micron scale, suggesting localized brittle deformation (Fig. 5c). However, dolomite micrograins do not show sharp angular boundaries, as expected in the case of pure brittle process, but display strongly anhedral and lobate habits, indicating preferential reaction at grain boundaries (Fig. 5d). Fig. 5e shows a detail of a dolomite micrograin, which is partially reacted and replaced by an ultrafine material. Anhedral dolomite grains are also characterized by the occurrence of abundant pores and vesicles, often showing preferential localization along cleavage surfaces or twinning planes, i.e. those sites where the crystal structure of dolomite is reasonably more stressed and reactive (e.g., Fig. 5f and g). Dolomite anhedral micrograins are enclosed in an ultrafine matrix, characterized by the widespread occurrence of vesicles, skeletal and acicular crystals, (Fig. 5h) as well as of apparently amorphous “bridges” among nearby dolomite micrograins. Similar microstructures have been already described in previous studies on carbonate deformation at seismic rate, both in natural seismogenic fault rocks and in experimentally deformed samples through high-velocity tests (e.g., Collettini et al., 2013; Mitchell et al., 2015). Most of the microstructures described above, are interpreted as the consequence of decarbonation processes due to frictional heating during seismic-rate deformation.

To further verify the possible occurrence of decarbonation process, we have performed a TEM investigation on Ar^{+} ion milled samples of the MFS (e.g., Fig. 7a). Approaching the MFS, dolomite crystals of the host dolostone exhibit subgrain boundaries and grain size reduction. The resulting grains have highly lobate, fading grain boundaries (Fig. 7b). Pores and vesicles are abundant, occurring both at grain boundaries (e.g., inset in Fig. 7b) and within dolomite crystal structure, as shown in Fig. 7c, where regular dolomite lattice fringes are « overlapped » to nanosized rounded vesicles.

TEM observation at the MFS (electron-transparent portions at the dashed line in Fig. 7a) revealed unique and surprising nanotextures (Fig. 8). In particular, dolomite crystals are characterized by an extremely high density of dislocations, giving rise to strain contrast features preferentially oriented perpendicular to the grain boundaries (dashed white lines in Fig. 8a–c). Dolomite crystals have extremely sharp and regular boundaries and are systematically surrounded by an ultrafine « envelope », 200–500 nm thick, followed by low-contrast film (Fig. 8a–c). Selected area electron diffraction (SAED), coupled with EDS data (see below), showed that the ultrafine envelope consists of randomly oriented, Mg-rich calcite nanograins, whereas the low-contrast film corresponds to an amorphous material with alumosilicate composition. We suggest that the alumosilicate material may derive from dehydration and decomposition of original layer silicates. This is supported by high-resolution images, showing relict (001) flakes of illite-muscovite within the amorphous material (e.g., the thin dark-contrast features in the upper side of Fig. 8c). We also remark the common concentration of voids at the boundary between alumosilicate material and Mg-rich calcite (e.g., bright portions in Fig. 8b and c). Fig. 8d–f reports the EDS spectra collected on the three different sites, confirming the sharp drop in Mg content within the ultrafine envelope and the possible phyllosilicate origin of the alumosilicate amorphous material (as testified by the occurrence of Al and K).

Fig. 9 reports a detail of the ultrafine Mg-rich calcite, commonly associated with vesicle-rich amorphous material (Fig. 9a). Single nanograins are round-shaped and smaller than 10 nm in size. Both the orientation of lattice fringes in HR- images and corresponding SAED pattern characterized by ring-shaped diffraction effects (inset) testify that nanograins are randomly oriented (Fig. 9b). We remark that a similar nanostructure can be hardly produced by simple brittle

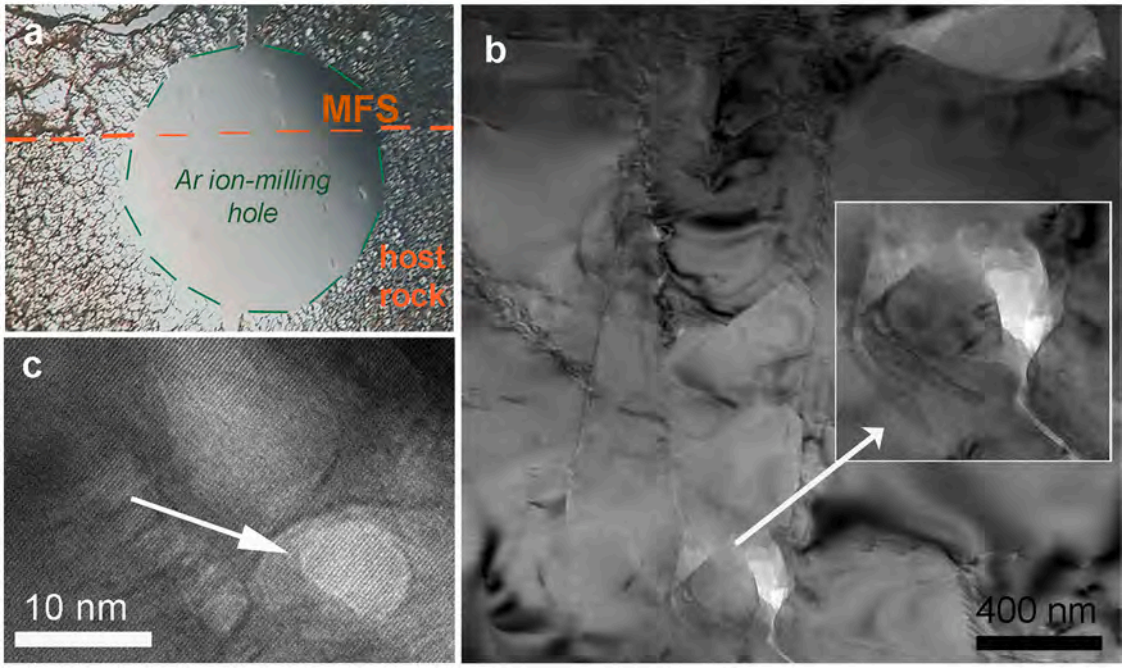

Fig. 7. (a) Representative Ar^{+} ion milled TEM sample (plane polarized light image), with electron-transparent portions in dolostone host rock, MFS and coarse dolomite vein (upper portion). (b) Deformed dolomite crystals with subgrain boundaries and grain size reduction; note the highly anhedral boundaries of dolomite nanograins (inset), commonly associated with voids. (c) Dolomite crystal, with regular lattice fringes, with inner vesicles and bubbles (light contrast). Bright-field TEM images.

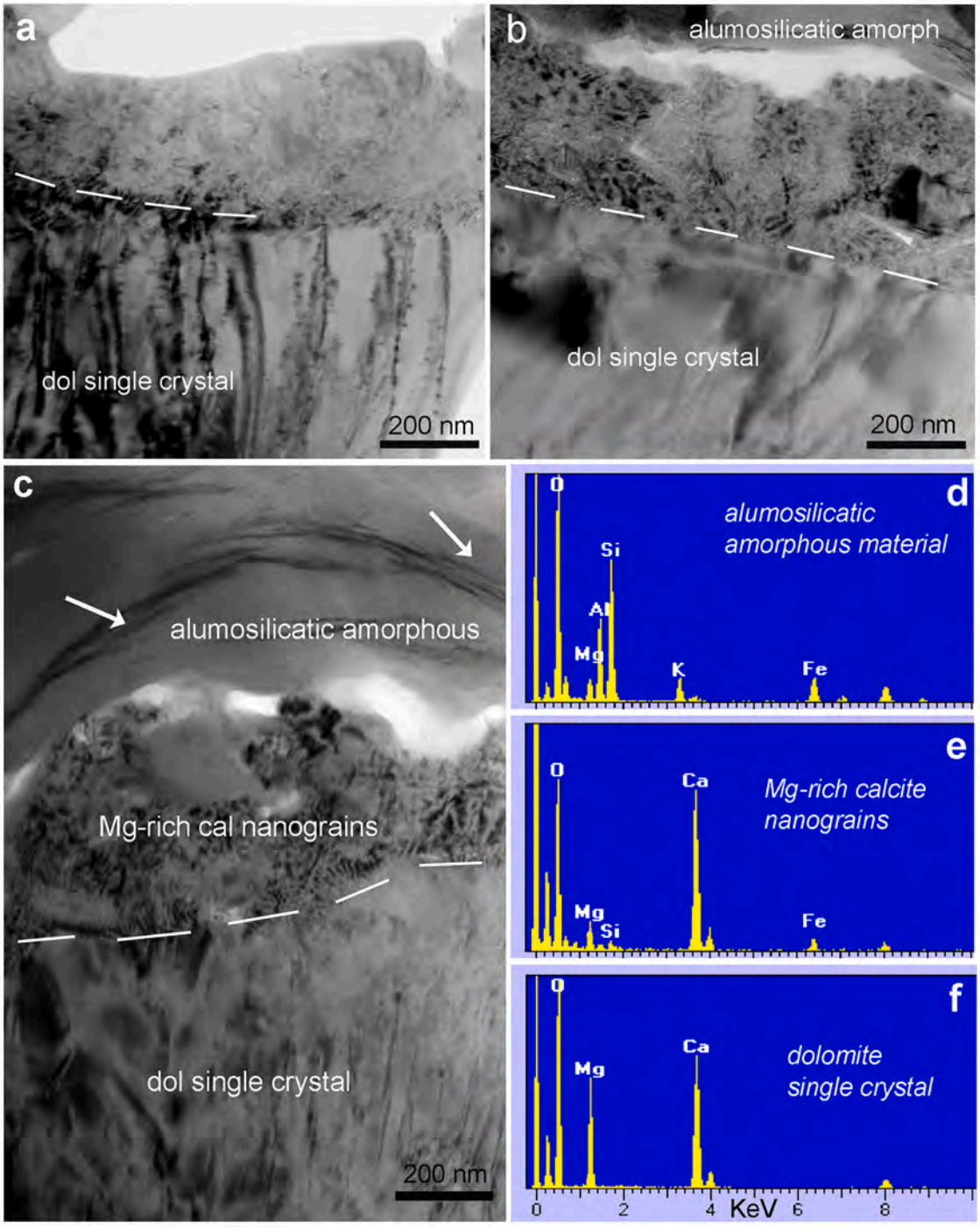

Fig. 8. Bright-field TEM images from the MFS. From (a) to (c) deformed dolomite crystals, with strain contrast features perpendicular to the sharp grain boundary (dashed white lines). Dolomite crystals are systematically surrounded by Mg-rich calcite nanograins and by an amorphous to poorly crystalline material with alumosilicate composition (see Fig. 4a In Viti, 2011, for a comparison with high-velocity, experimentally deformed dolomite). Dark lamellar features within the amorphous alumosilicate material (e.g., white arrows in c) correspond to crystalline relics of illite-mica layer silicates. Figures (d), (e) and (f) show representative EDS spectra of amorphous material (d), Mg-rich calcite nanograins (e) and strained dolomite (f), respectively. Signals at ~ 0.2 and 8 KeV are due to carbon coating and to Cu grid contributions, respectively.

fracturing and grain size reduction, whereas it strongly suggests possible amorphization and subsequent recrystallization. Measured d-spacings, coupled with EDS data on these aggregates, confirm that nanocrystals correspond to Mg-rich calcite. The above TEM images are in excellent agreement with TEM observations on experimentally deformed dolomite in high-velocity test (see, for direct comparison, Fig. 4a and b in Viti 2011 and Fig. 2F and G in De Paola et al. 2011).

6. Discussion and conclusions

6.1. *"Hidden earthquakes" in dolostones*

Earthquake-induced decomposition of carbonatic rocks due to frictional heating along faults is a common process, but difficult to be detected from field investigations alone ("hidden earthquakes").

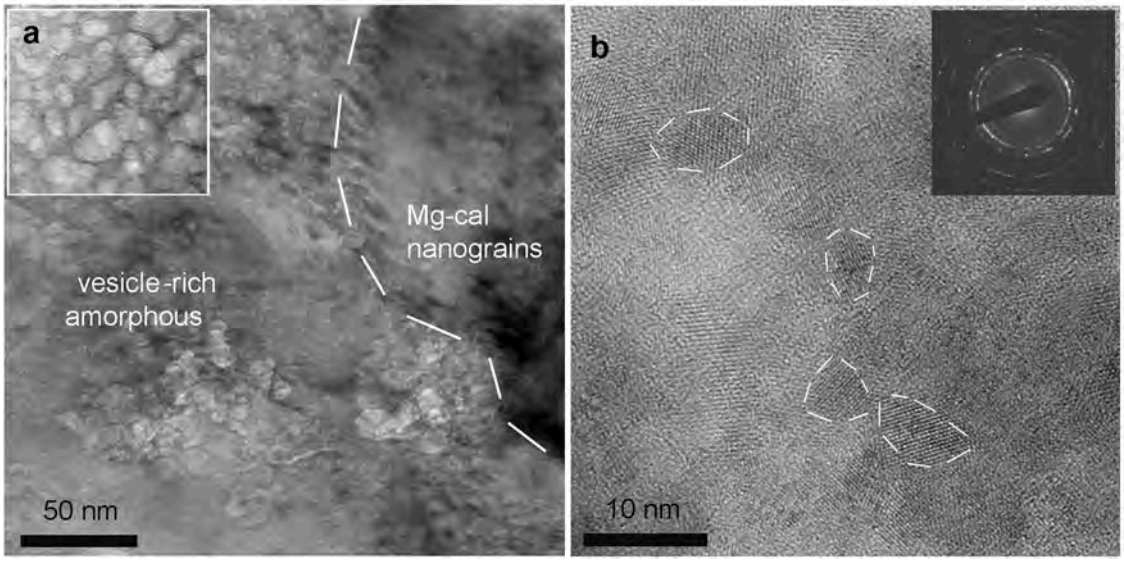

Fig. 9. (a) Bright-field TEM image from the MFS, showing the abundance of vesicles and pores within the alumosilicatic amorphous material occurring close to the randomly oriented Mg-rich calcite nanograins. (b) High-resolution image of the Mg-rich calcite nanograins. Dashed lines highlight single nanograins, less than 10 nm in size, showing variably oriented lattice fringes (corresponding ring-shaped SAED pattern in the inset). HR image can be compared with Fig. 4b in Viti (2011) and *Fig. 2g* in De Paola et al. (2011), showing dolomite decomposition products during high-velocity deformation tests.

Whereas evidence of seismic thermal decomposition in limestone is increasingly reported in the literature (e.g., Tesei et al., 2013; Collettini et al., 2013, 2014; Coppola et al., 2021; Ohl et al., 2020) there is still limited documentation for dolostone.

Notable examples of dolostone thermal decomposition are scarce. Rowe et al. (2012) first reported the occurrence of dolostone decomposition associated to a fault zone. Their evidence is mostly based on the fluidized and laminated fabric of dolomite cataclasite along the Naukluft thrust and, at the microscale, appearance of rounded clasts, with abundant pores, similarly to high-velocity friction experiments (Rowe et al., 2012). Similar evidence of dolostone decarbonation were proposed about the shear zone at the base of the Heart mountain giant landslide (Mitchell et al., 2015), in which decomposed dolomite grains were observed in a calcite-rich matrix within the basal fluidized cataclasite. In both cases, the potentially decarbonated cataclasite was not unambiguously related to a seismogenic fault.

In the case of the seismogenic DFZ, we show unequivocal evidence of dolomite and phyllosilicate thermal decarbonation along fault surfaces that are kinematically consistent with the earthquake moment tensor (Fig. 10a). Decomposition microstructures of dolomite, such as anhedral grain boundaries and abundance of pores and vesicles, are highlighted at the SEM scale, (Fig. 5). Additional clues of intense strain and fast slip are supported by EBSD results: i) the random crystallographic orientation of the grains in the MFS supports grain size reduction having been caused by fast fracturing and rotation of the clasts (cataclasis); ii) grain boundary sliding has likely occurred by "superplastic" mechanisms analogous to those documented in high-velocity tests by Pozzi et al. (2021) as suggested by four-grain-contacts in the microstructures; iii), patches of "smaller grains" with open spaces may be the equivalent of grain size reduction mechanism to < 1 μm as documented within

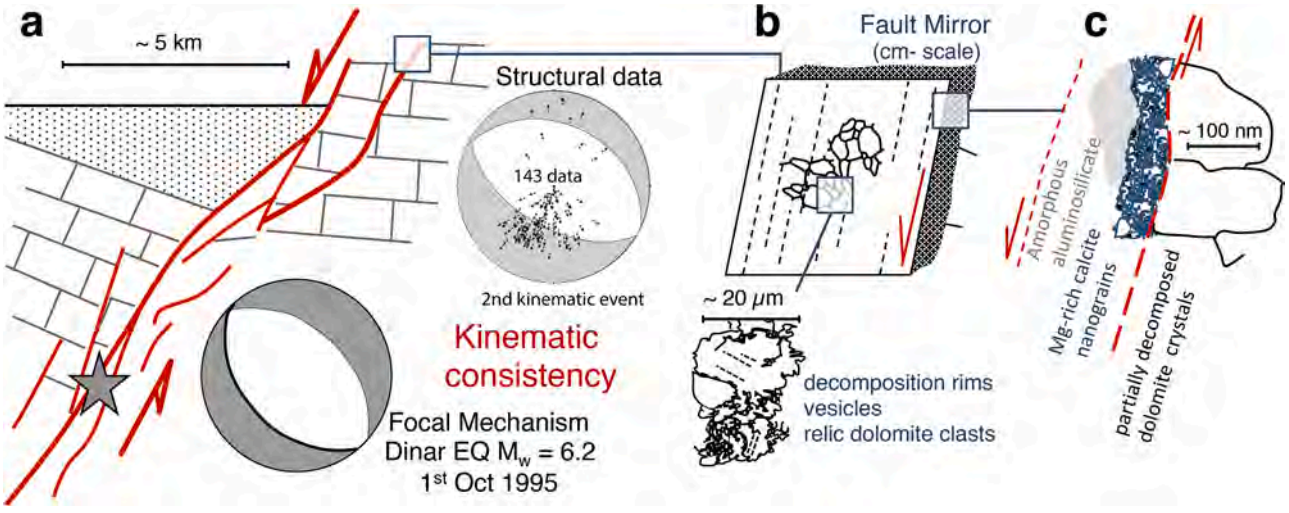

Fig. 10. Multiple indicators of co-seismic decarbonation along the Dinar Fault surface (fault sketch not to scale). (a) Kinematic consistency among of field structural indicators (fault planes and lineations) and Dinar Earthquake focal mechanism yielding similar stress tensors. (b) Reflective striated fault mirrors at the cm scale highlight extreme localization of the fault plane. At the micron scale, dolomite in the MFS has decomposition rims and vesicles at grain boundaries and inside the grains. (c) At the nanoscale, dolomite is replaced by its high-T decomposition product, i.e., nanogranular Mg-rich calcite, typically associated with an aluminosilicate amorphous material, deriving from phyllosilicate clast decomposition.

(Fig. 5); iv) stereography does not explain the binary grain size distribution within the MFS.

Another key line of evidence is the nanocrystalline layer found at the contact between the cemented cataclasite and the fault vein, which can be interpreted as the remnant of a thermally decomposed principal slip zone, with a late overprinting due to the opening and filling of the fault plane crack. The slip zone is mineralogically and texturally distinct from the surrounding rock, showing highly strained dolomite grains associated with Mg-rich calcite nanocrystals, vesicles and amorphous alumosilicate material (Figs. 8 and 9).

In addition, at the outcrop and hand sample scale, the fault plane is a reflective surface, a fault mirror, like those documented in the literature (e.g. Fondriest et al., 2013; Chinello et al., 2023). Even if the fault mirror is not unambiguous evidence of seismic frictional heating along the fault plane, its association with the nanocrystalline slip zone is a further confirmation of intense strain along, a pre-requisite for efficient seismic localization.

We conclude that the dolomite decarbonation along the Dinar MFZ is induced by a localized T increase due to frictional heating in and/or near the MFZ, consistently with previous HV experimental and natural fault samples showing nanocrystalline slip zones (e.g., De Paola et al. 2011; Fondriest et al., 2013; Smith et al., 2017), particularly in presence of dolomite and calcite-dolomite mixtures (Fondriest et al., 2013; Smith et al., 2017; Demurtas et al., 2019). In several of these experiments, the principal slip zones are often associated to a fault mirror and built by Mg-rich calcite nanograins, sometimes with periclase (e.g., Fondriest et al., 2013; Demurtas et al., 2019).

Definitely, the documentation of dolomite thermal decomposition in natural faults is rare and potentially overlooked. We suggest that, to identify seismic-induced thermal decomposition in dolostone-built faults, several indicators should be found together (Fig. 10), instead of relying on single microstructural evidence: both bulk information from fluidized and/or decomposed cataclasite (Rowe et al., 2012; Mitchell et al., 2015; this study Fig. 10b) should be combined with smaller scale evidence from fault mirrors (Fondriest et al., 2013; Chinello et al., 2023) together with nanocrystalline Mg-calcite occurrences (this study Fig. 10c, Coppola et al., 2021).

6.2. Dolomite decarbonation and the fate of periclase in fault rocks

Dolomite decomposition is usually described as a two-stage process (e.g., Kok et al. 2008; Resio 2024 and reference therein), starting at ~ 550 °C, with two main mass loss episodes at 690–810 and 810–920 °C, that are, respectively:

$CaMg(CO_3)_2 \rightarrow CaCO_3 + MgO + CO_2$ mass loss of ~ 24 %

$CaCO_3 \rightarrow CaO + CO_2$ final mass loss of ~ 47 %.

Based on our SEM and TEM results, the second stage (involving calcite decarbonation) did not occur, constraining frictional heating to a maximum T of ~ 800 °C.

A recent review of dolomite thermal behavior (Resio, 2024) underlines that, although the nature of the final high-temperature products is certain (MgO and CaO), there are conflicting theories about the number of thermal decomposition stages, the nature of intermediate products, as well as decomposition peak temperatures. This inconsistent picture depends on many factors, among which dolomite grain size, oxidizing conditions and fluid chemistry, pressure and extent of deformation. We remark that, in our case, dolomite decomposition takes place within a fault zone, i.e., a highly dynamic, anisotropic and heterogeneous system, where different processes may interplay and overlap each other (Fig. 10b,a). In particular, the exact definition of decarbonation temperatures and products may be strongly dependent on specific fault-related processes such as ultracomminution, intracrystalline deformation, subgrain boundaries, mass loss, fluid release and circulation, formation of amorphous or nanosized phases and fluidization.

Another key feature when dealing with fault zone decarbonation reactions is the consistent mass loss (up to 24 % for the first stage of dolomite reaction) and subsequent CO_2 release, which potentially lower the effective normal stress of the fault (Sulem and Famin, 2008). The availability of CO_2 within the deformation zone, coupled with localized fluid circulation dynamics, is fundamental to understand the mineralogical evolution of the fault rocks, in particular for what concerns possible re-carbonation and/or hydration reactions of the high-temperature products (CaO and MgO, both very reactive).

We remark that periclase (MgO) has been never detected in natural seismic fault rocks, even in our Dinar fault samples. This poses a question about the preservation of periclase along thermally decomposed seismic fault surfaces. According to Caceres & Attiogbe (1997), in presence of water, the chemically active MgO immediately transform in $Mg(OH)_2$, that may evolve into water soluble Mg bicarbonate. Preferential circulation of fluids within the deformed zone reasonably provides the water amount required to bring into solution all the available Mg bicarbonate, thus explaining why MgO is rarely or never observed in decarbonated dolomite in natural fault rocks.

6.3. Earthquakes in the seismogenic volume of the dinar fault

The fault mirror we studied in this work represents only one of the several outstanding fault surfaces exposed in the area of the Mw = 6.2, 1995 Dinar Earthquake. The fault zone is represented by several fault segments containing both sub-parallel and overlapping principal slip surfaces, each accommodating different displacements. This fault system can be activated simultaneously during an earthquake sequence, as highlighted by high-resolution aftershock location during major earthquakes (e.g., Valoroso et al., 2014; Ross et al., 2019; Collettini et al., 2022; Shelly et al., 2023). It implies that during exhumation and throughout several seismic cycles, even small displacement fault surfaces have the potential to record seismic slip, effectively becoming a powerful tool to reveal seismogenic faults and fault volumes in the geologic record.

To test this hypothesis, we can compute the amount of frictional heating that we can expect on thin fault surfaces during a seismic sequence, assuming that the 1995 Dinar sequence is representative of the typical seismic cycle along these major seismogenic volumes. The Dinar fault experienced several seismic cycles in historical times characterized by $M > 6$ earthquakes (Ozalp et al., 2018). During the 1995 sequence, the Mw 6.2 mainshock was preceded by more than 30 foreshocks of magnitude $3 < M_l < 4.8$ and was followed by a long aftershock sequence with several events $4 < M_l < 5$ occurring between 0 - 25 km depth (Pınar, 1998, Öncel et al., 2014).

If the normal faults belonging to the Dinar fault seismogenic volume dip ~60°, and assuming a vertical σ_1, we can compute the minimum normal stress on the fault surfaces as to be $\sigma_v * \sin(30) = 13.5$ MPa/km, considering a mean rock density of 2700 kg/m^3. Following Rice (2006), we can estimate the temperature rise on thin fault planes as $\Delta T = (\tau/\rho C_p)(Vd/\pi\alpha_{th})^{1/2}$, where τ is the shear stress on the fault plane, ρC_p the heat capacity per unit volume, V is the slip velocity of rocks along the fault, d the mean fault slip and α_{th} the thermal diffusivity of the rock. We assume a Coulomb-type frictional strength of the rocks, with friction coefficient of ~0.6, C = 962 J/kgK, ρ= 2700 kg/m3, and thermal diffusivity of carbonates $\alpha_{th} = 1.3 \times 10^{-6}$ m^2/s (Billi and Di Toro, 2008) and constant slip velocity $V = 1$ m/s (Heaton, 1990). At 1 km depth, a seismic slip of ~0.2 m is sufficient to trigger dolostone decomposition reactions ($\Delta T > 550$ °C), roughly equivalent to the mean slip occurring during a M 5–6 earthquake (Wells and Coppersmith, 1994). At 3 km depth, the maximum depth at which we can expect dolostone host rocks, fault slips as small as 4 cm, equivalent to ~M 4 earthquakes (Sibson, 1989; Wells and Coppersmith, 1994), can induce thermal decomposition along thin slip zones of dolostone-built faults.

These estimates, combined with our micro- and nano-structural observations and the record of past seismicity along the Dinar Fault Zone, demonstrate the potential of preservation of ancient seismic cycles in complex fault systems with multiple slip surfaces, potentially including

the record foreshocks and aftershocks.

This study highlights the crucial role of integrated meso- to nano-structural analysis of fault rocks to identify seismic slip indicators, and it reports one of the most unambiguous examples of earthquake-induced dolomite decarbonation along dolostone-hosted fault planes (Fig. 10).

Submission declaration we declare that:

- the work above has not been published previously;
- the article is not under consideration for publication elsewhere;
- the article's publication is approved by all authors and tacitly or explicitly by the responsible authorities where the work was carried out;
- if accepted, the article will not be published elsewhere in the same form, in English or in any other language, including electronically, without the written consent of the copyright-holder.

Figure for the supplementary material: Fig. 1 s - Location of the structural stations within the Dinar Fault System and where kinematic data on fault segments were collected (after Alçiçek et al. 2013). The study highlighted two main kinematic events, the first transtensional and the second normal, as shown by the stereonets. Assuming that the measured slickelines are parallel to the main shear stress, then kinematic and geometrical data from fault surfaces are used to get paleo-stress analysis, graphically represented by double-couple fault-plane solution diagrams, of which the one related to the second kinematic event shows similitude with the focal mechanism of the Dinar earthquake (after Pınar, 1998), as reported in the legend. The location of the borehole Ç33 is also indicated: this drilled 648 m of Quaternary sediments without reaching the substratum after (Sezgin, 2020). The data related to the ground vertical movements are from Wright et al. (1999).

CRediT authorship contribution statement

Cecilia Viti: Writing – original draft, Methodology, Investigation, Data curation, Conceptualization. **Telemaco Tesei:** Writing – original draft, Validation, Formal analysis, Data curation. **Andrea Brogi:** Writing – original draft, Methodology, Investigation, Data curation, Conceptualization. **Richard Spiess:** Writing – original draft, Methodology, Investigation, Data curation. **Domenico Liotta:** Writing – original draft, Methodology, Investigation, Data curation. **M. Cihat Alçiçek:** Writing – original draft, Resources, Investigation.

Declaration of competing interest

None.

Acknowledgments

TT acknowledges the support of the Italian Ministry of Education, University and Research through the PRIN project 2022XBCW58 (“FASTHEAL”). The field studies were supported by TÜBİTAK (Turkish Research and Technological Council) with grant number of ÇAY-DAG105Y280. RS acknowledges grants of the University of Padova for access to EBSD-Symmetry2 equipped Solaris FEG-FIB SEM at the Department of Geosciences. AB received funding from the Italian Ministry of University and Research through the PNNR Mission 4 - Component 2 - Investment 1.1 Project PRIN-PNNR2022 no. P2022KKJ55.

We also acknowledge the two anonymous referees whose suggestions greatly improved the paper.

Supplementary materials

Supplementary material associated with this article can be found, in the online version, at doi:10.1016/j.epsl.2026.120030.

Data availability

No data was used for the research described in the article.

References

Alçiçek, M.C., Brogi, A., Capezzuoli, E., Liotta, D., Meccheri, M., 2013. Superimposed basin formation during Neogene-Quaternary extensional tectonics in SW-Anatolia (Türkiye): insights from the kinematics of the Dinar Fault Zone. Tectonophysics 608, 713–727. https://doi.org/10.1016/j.tecto.2013.08.008.

Bernard, P., Lyon-Caen, H., Briole, P., Deschamps, A., Boudin, F., Makropoulos, K., Papadimitriou, P., Lemeille, F., Patau, G., Billiris, H., Paradissis, D., 2006. Seismicity, deformation and seismic hazard in the western rift of Corinth: new insights from the Corinth Rift Laboratory (CRL). Tectonophysics 426, 7–30. https://doi.org/10.1016/j.tecto.2006.02.012.

Beutner, E.C., Gerbi, G.P., 2005. Catastrophic emplacement of the Heart Mountain block slide, Wyoming and Montana, USA. Geol. Soc. Am. Bull. 117 (5). https://doi.org/10.1130/B25451.

Billi, A., Di Toro, G. and Landowe, S.J., 2008. Fault-related carbonate rocks and earthquake indicators: recent advances and future trends. In *Structural Geology: New Research*, pp.63–86. ISBN 978-1-60456-827-1.

Burchfiel, B.C., Royden, L.H., Van der Hilst, R.D., Hager, B.H., Chen, Z., King, R.W., Li, C., Lü, J., Yao, H., Kirby, E., 2008. A geological and geophysical context for the Wenchuan earthquake of 12 May 2008, Sichuan, People's Republic of China. GSa Today 18, 4–11. https://doi.org/10.1130/GSATG18A.1.

Caceres, P.G., Attiogbe, E.K., 1997. Thermal decomposition of dolomite and the extraction of its constituents. Miner. Eng. 10, 1165–1176. https://doi.org/10.1016/S0892-6875(97)00101-5.

Chinello, M., Bersan, E., Fondriest, M., Tesei, T., Gomila, R., Di Toro, G., 2023. Seismic cycle in bituminous dolostones (Monte CAMICIA thrust zone, central Apennines, Italy). Geochem. Geophys. Geosyst. 24, e2023GC011063. https://doi.org/10.1029/2023GC011063.

Collettini, C., Viti, C., Tesei, T., Mollo, S., 2013. Thermal decomposition along natural carbonate faults during earthquakes. Geology 41, 927–930. https://doi.org/10.1130/G34421.1.

Collettini, C., Carpenter, B.M., Viti, C., Cruciani, F., Mollo, S., Tesei, T., Trippetta, F., Valoroso, L., Chiaraluce, L., 2014. Fault structure and slip localization in carbonate-bearing normal faults: an example from the Northern Apennines of Italy. J. Struct. Geol. 67, 154–166. https://doi.org/10.1016/j.jsg.2014.07.017.

Collettini, C., Barchi, M.R., De Paola, N., Trippetta, F., Tinti, E., 2022. Rock and fault rheology explain differences between on fault and distributed seismicity. Nat. Commun. 13, 5627. https://doi.org/10.1038/s41467-022-33373-y.

Coppola, M., Correale, A., Barberio, M.D., Billi, A., Cavallo, A., Fondriest, M., Nazzari, M., Paonita, A., Romano, C., Stagno, V., Viti, C., 2021. Meso-to nano-scale evidence of fluid-assisted co-seismic slip along the normal Mt. Morrone Fault, Italy: implications for earthquake hydrogeochemical precursors. Earth Planet. Sci. Lett. 568, 117010. https://doi.org/10.1016/j.epsl.2021.117010.

De Paola, N., Hirose, T., Mitchell, T., Di Toro, G., Viti, C., Shimamoto, T., 2011. Fault lubrication and earthquake propagation in thermally unstable rocks. Geology 39, 35–38. https://doi.org/10.1130/G31398.1.

Demurtas, M., Smith, S.A., Prior, D.J., Spagnuolo, E., Di Toro, G., 2019. Development of crystallographic preferred orientation during cataclasis in low-temperature carbonate fault gouge. J. Struct. Geol. 126, 37–50. https://doi.org/10.1016/j.jsg.2019.04.015.

Dingley, D., 2004. Progressive steps in the development of electron backscatter diffraction and orientation imaging microscopy. J. Microsc. 213, 214–224. https://doi.org/10.1111/j.0022-2720.2004.01321.x.

Fondriest, M., Smith, S.A., Candela, T., Nielsen, S.B., Mair, K., Di Toro, G., 2013. Mirror-like faults and power dissipation during earthquakes. Geology 41, 1175–1178. https://doi.org/10.1130/G34641.1.

Griffith, W.A., Nielsen, S., Di Toro, G., Smith, S.A., 2010. Rough faults, distributed weakening, and off-fault deformation. J. Geophys. Res.: Solid Earth 115 (B8). https://doi.org/10.1029/2009JB006925, 115(B8).

Han, R., Hirose, T., Shimamoto, T., 2010. Strong velocity weakening and powder lubrication of simulated carbonate faults at seismic slip rates. J. Geophys. Res.: Solid Earth 115 (B3). https://doi.org/10.1029/2008JB006136.

Heaton, T.H., 1990. Evidence for and implications of self-healing pulses of slip in earthquake rupture. Phys. Earth Planet. Inter. 64 (1), 1–20.

Kirkpatrick, J.D., Rowe, C.D., White, J.C., Brodsky, E.E., 2013. Silica gel formation during fault slip: evidence from the rock record. Geology 41, 1015–1018. https://doi.org/10.1130/G34483.1.

Kok, M., Smykatz-Kloss, W., 2008. Characterization, correlation and kinetics of dolomite samples as outlined by thermal methods. J. Therm. Anal. Calorim. 91 (2), 565–568. https://doi.org/10.1007/s10973-007-8560-3.

Koral, H., 2000. Surface rupture and rupture mechanism of the October 1, 1995 (Mw = 6.2) Dinar earthquake, SW Türkiye. Tectonophysics 327, 15–24. https://doi.org/10.1016/S0040-1951(00)00159-1.

Mitchell, T.M., Smith, S.A., Anders, M.H., Di Toro, G., Nielsen, S., Cavallo, A., Beard, A. D., 2015. Catastrophic emplacement of giant landslides aided by thermal decomposition: heart Mountain, Wyoming. Earth Planet. Sci. Lett. 411, 199–207. https://doi.org/10.1016/j.epsl.2014.10.051.

Ohl, M., Plümper, O., Chatzaras, V., Wallis, D., Vollmer, C., Drury, M., 2020. Mechanisms of fault mirror formation and fault healing in carbonate rocks. Earth Planet. Sci. Lett. 530, 115886. https://doi.org/10.1016/j.epsl.2019.115886.

Öncel, A.O., Koral, H., Alptekin, Ö., 1998. The Dinar Earthquake (Mw = 6.2; October 1, 1995; Afyon-Türkiye) and Earthquake Hazard of the Dinar-Çivril Fault. Pure Appl. Geophys. 152, 91–105. https://doi.org/10.1007/s000240050143.

Özalp, S., Emre, Ö., ŞaroŞlu, F., Özaksoy, V., Elmacı, H., Duman, T.Y., 2018. Active fault segmentation of the Çivril Graben System and surface rupture of the 1 October 1995 Dinar earthquake (Mw 6.2), Southwestern Anatolia, Türkiye. J. Asian Earth. Sci. 166, 136–151. https://doi.org/10.1016/j.jseaes.2018.07.037.

Pearce, M.A., Timms, N.E., Hough, R.M., Cleverley, J.S., 2013. Reaction Mechanism for the Replacement of Calcite by Dolomite and Siderite: implications for Geochemistry, Microstructure and Porosity Evolution during Hydrothermal Mineralisation. Contribut. Mineral. Petrol. 166, 995–1009. https://doi.org/10.1007/s00410-013-0905-2.

Pinar, A., 1998. Source inversion of the October 1, 1995, Dinar earthquake (Ms = 6.1): a rupture model with implications for seismotectonics in SW Türkiye. Tectonophysics 292, 255–266.

Platevoet, B., Scaillet, S., Guillou, H., Blamart, D., Nomade, S., Massault, M., Poisson, A., Elitok, Ö., Özgür, N., Yağmurlu, F., Yılmaz, K., 2008. Pleistocene eruptive chronology of the Gölcük volcano, Isparta Angle, Türkiye. Quaternaire 19, 147–156. https://doi.org/10.4000/quaternaire.3092.

Power, W.L., Tullis, T.E., 1989. The relationship between slickenside surfaces in fine-grained quartz and the seismic cycle. J. Struct. Geol. 11, 879–893. https://doi.org/10.1016/0191-8141(89)90105-3.

Pozzi, G., De Paola, N., Nielsen, S.B., Holdsworth, R.E., Tesei, T., Thieme, M., Demouchy, S., 2021. Coseismic fault lubrication by viscous deformation. Nat. Geosci. 14, 437–442. https://doi.org/10.1038/s41561-021-00747-8.

Pozzi, G., De Paola, N., Holdsworth, R.E., Bowen, L., Nielsen, S.B., Dempsey, E.D., 2019. Coseismic ultramylonites: an investigation of nanoscale viscous flow and fault weakening during seismic slip. Earth Planet. Sci. Lett. 516, 164–175. https://doi.org/10.1016/j.epsl.2019.03.042.

Rau, E.I., Reimer, L., 2001. Fundamental problems of imaging subsurface structures in the backscattered electron mode in scanning electron microscopy. Scanning 23, 235–240. https://doi.org/10.1002/sca.4950230403.

Resio, L.C., 2024. Dolomite thermal behavior: a short review. Phys. Chem. Miner. 51, 19. https://doi.org/10.1007/s00269-024-01272-x.

Rice, J.R., 2006. Heating and weakening of faults during earthquake slip. J. Geophys. Res.: Solid Earth 111 (B5). https://doi.org/10.1029/2005JB004006.

Ross, Z.E., Idini, B., Jia, Z., Stephenson, O.L., Zhong, M., Wang, X., Zhan, Z., Simons, M., Fielding, E.J., Yun, S.H., Hauksson, E., 2019. Hierarchical interlocked orthogonal faulting in the 2019 Ridgecrest earthquake sequence. Science (1979) 366 (6463), 346–351.

Rowe, C.D., Fagereng, Å., Miller, J.A., Mapani, B., 2012. Signature of coseismic decarbonation in dolomitic fault rocks of the Naukluft Thrust, Namibia. Earth Planet. Sci. Lett. 333, 200–210. https://doi.org/10.1016/j.epsl.2012.04.030.

Rowe, C.D., Griffith, W.A., 2015. Do faults preserve a record of seismic slip: a second opinion. J. Struct. Geol. 78, 1–26. https://doi.org/10.1016/j.jsg.2015.06.006.

Sezgin, M., 2020. Çivril Graben Sisteminde (Denizli-Afyonkarahisar) Yer Alan Ruhsat Sahalarına Ait Kömür Aramaları Jeoloji Raporu. Scientific Report No.14411. Mineral Research and Exploration Directorate of Türkiye (MTA), Ankara, p. 20.

Shelly, D.R., Skoumal, R.J., Hardebeck, J.L., 2023. Fracture-mesh faulting in the swarm-like 2020 Maacama sequence revealed by high-precision earthquake detection, location, and focal mechanisms. Geophys. Res. Lett. 50 (1), 2022GL101233.

Sibson, R.H., 1989. Earthquake faulting as a structural process. J. Struct. Geol. 11, 1–14. https://doi.org/10.1016/0191-8141(89)90032-1.

Smith, S.A.F., Di Toro, G., Kim, S., Ree, J.H., Nielsen, S., Billi, A., Spiess, R., 2013. Coseismic recrystallization during shallow earthquake slip. Geology 41 (1), 63–66.

Smith, S.A., Griffiths, J.R., Fondriest, M., Di Toro, G. 2017. "Coseismic foliations" in gouge and cataclasite: experimental observations and consequences for interpreting the fault rock record. In: *Fault Zone Dynamic Processes: Evolution of Fault Properties During Seismic Rupture* pp.81–102. https://doi.org/10.1002/9781119156895.ch5.

Siman-Tov, S., Aharonov, E., Sagy, A., Emmanuel, S., 2013. Nanograins form carbonate fault mirrors. Geology 41, 703–706. https://doi.org/10.1130/G34087.1.

Sulem, J., Famin, V., 2009. Thermal decomposition of carbonates in fault zones: slip-weakening and temperature-limiting effects. J. Geophys. Res.: Solid Earth 114 (B3). https://doi.org/10.1029/2008JB006004.

Ten Veen, J.H., Boulton, S.J., Alçiçek, M.C., 2009. From palaeotectonics to neotectonics in the Neotethys realm: the importance of kinematic decoupling and inherited structural grain in SW Anatolia (Türkiye). Tectonophysics 473, 261–281. https://doi.org/10.1016/j.tecto.2008.09.030.

Tesei, T., Collettini, C., Viti, C., Barchi, M.R., 2013. Fault architecture and deformation mechanisms in exhumed analogues of seismogenic carbonate-bearing thrusts. J. Struct. Geol. 55, 167–181. https://doi.org/10.1016/j.jsg.2013.07.007.

Tesei, T., Carpenter, B.M., Giorgetti, C., Scuderi, M.M., Sagy, A., Scarlato, P., Collettini, C., 2017. Friction and scale-dependent deformation processes of large experimental carbonate faults. J. Struct. Geol. 100, 12–23. https://doi.org/10.1016/j.jsg.2017.05.008.

Utkucu, M., Pinar, A., Alptekin, Ö., 2002. A detailed slip model for the 1995, October 1, Dinar, Türkiye, earthquake (MS= 6.1) determined from inversion of teleseismic P and SH waveforms. Geophys. J. Int. 151, 184–195. https://doi.org/10.1046/j.1365-246X.2002.01763.x.

Valoroso, L., Chiaraluce, L., Collettini, C., 2014. Earthquakes and fault zone structure. Geology 42, 343–346. https://doi.org/10.1130/G35071.1.

Verberne, B.A., Plümper, O., Matthijs de Winter, D.A., Spiers, C.J., 2014. Superplastic nanofibrous slip zones control seismogenic fault friction. Science (1979) 346, 1342–1344. https://doi.org/10.1126/science.1259003.

Viganò, A., Tumiati, S., Recchia, S., Martin, S., Marelli, M., Rigon, R., 2011. Carbonate pseudotachylytes: evidence for seismic faulting along carbonate faults. TerraNova 23 (3), 187–194. https://doi.org/10.1111/j.1365-3121.2011.00997.

Viti, C., 2011. Exploring fault rocks at the nanoscale. *Review paper*. J. Struct. Geol. 33, 1715–1727. https://doi.org/10.1016/j.jsg.2011.10.005.

Wells, D.L., Coppersmith, K.J., 1994. New empirical relationships among magnitude, rupture length, rupture width, rupture area, and surface displacement. Bull. Seismolog. Soc. Am. 84 (4), 974–1002.

Westaway, R., Pringle, M., Yurtmen, S., Demir, T., Bridgland, D., Rowbotham, G., Maddy, D., 2004. Pliocene and Quaternary regional uplift in western Turkey: the Gediz River terrace staircase and the volcanism at Kula. Tectonophysics 391, 121–169. https://doi.org/10.1016/j.tecto.2004.07.013.

Wright, T.J., Parsons, B.E., Jackson, J.A., Haynes, M., Fielding, E.J., England, P.C., Clarke, P.J., 1999. Source parameters of the 1 October 1995 Dinar (Turkey) earthquake from SAR interferometry and seismic bodywave modelling. EPSL 172, 23–37.